

Holographic Representation of One-Dimensional Many-Body Quantum States via Isometric Tensor Networks

Kaito Kobayashi,^{1,*} Benjamin Sappler,^{2,3,*} and Frank Pollmann^{2,3}

¹*Department of Applied Physics, the University of Tokyo, 7-3-1 Hongo, Bunkyo-ku, Tokyo 113-8656, Japan*

²*Technical University of Munich, TUM School of Natural Sciences, Physics Department, 85748 Garching, Germany*

³*Munich Center for Quantum Science and Technology (MCQST), Schellingstr. 4, 80799 München, Germany*

(Dated: December 16, 2025)

Isometric tensor network states (isoTNS) allow for efficient and accurate simulations of higher-dimensional quantum systems by enforcing an isometric structure. We bring this idea back to one dimension by introducing a holographic isoTNS ansatz: a (1+1)-dimensional lattice of isometric tensors where the horizontal axis encodes physical space and an auxiliary “holographic” axis boosts expressivity. Despite the enlarged geometry, contractions and local updates remain computationally efficient due to isometric constraints. We investigate this ansatz and benchmark it in comparison to matrix product states (MPS). First, we show that randomly initialized holographic isoTNS typically display volume-law entanglement even at modest bond dimension, surpassing the representational limits of MPS and related ansätze. Second, through analytic constructions and variational optimization, we demonstrate that holographic isoTNS can faithfully represent arbitrary fermionic Gaussian states, Clifford states, and certain short-time-evolved states under local evolution—a family of states that is highly entangled but low in complexity. Third, to exploit this expressivity in broad situations, we implement a time-evolving block decimation (TEBD) algorithm on holographic isoTNS. While the method remains efficient and scalable, error accumulation over TEBD sweeps suppresses entanglement and leads to rapid deviations from exact dynamics. Overall, holographic isoTNS broaden the reach of tensor-network methods, opening new avenues to study physics in the volume-law regime.

I. INTRODUCTION

Quantum many-body physics lies at the heart of modern science, yielding emergent phenomena ranging from high-temperature superconductivity to exotic topological phases [1–3]. Yet the very source of that diversity—the exponential dimensionality of the many-body Hilbert space—makes a full description of quantum states notoriously difficult. Among the strategies devised to tame this complexity, tensor network representations have proven exceptionally fruitful [4]. In one dimension (1D) in particular, matrix product states (MPS) combined with density matrix renormalization group (DMRG) algorithms have become the gold standard for ground-state and low-energy calculations [5–12]. This efficiency, however, comes at the cost of restricting the accessible manifold of states: In terms of entanglement and complexity [13], MPS faithfully capture only weakly entangled (“area-law”) and low-complexity states. Extensions such as the multiscale entanglement renormalization ansatz (MERA) and tree tensor networks (TTN) broaden this reach to capture the critical (logarithmic) scaling of entanglement entropy [14–17]. Nevertheless, these approaches become inaccurate or prohibitively costly for (i) highly entangled (“volume-law”), high-complexity states—typically less physical in practice, as they arise only after exponentially long evolution times—and (ii) highly entangled yet low-complexity states of greater physical interest, such as short-time-evolved states [18–20].

A natural way to go beyond MPS is to enhance the network variational manifold by enlarging the network configuration; however, this quickly drives up the computational

cost. Useful guidance comes from isometric tensor network states (isoTNS), which efficiently represent two-dimensional (2D) quantum states [21–24]. In higher dimensions including 2D, the presence of internal loops makes exact network contraction exponentially costly [25–28]. IsoTNS mitigates this scaling by imposing isometric constraints on the tensors, such that many internal tensor contractions reduce to identity operations. Notably, a 1D tensor network with such isometric conditions is precisely an MPS in isometric form (sometimes also referred to as canonical form [29, 30]), which motivated the higher-dimensional extension to isoTNS. Here, we bring the isoTNS philosophy back to 1D: We present tensor networks with geometries richer than a simple chain, capable of representing certain highly entangled 1D quantum states.

In this work, we propose a “holographic” isoTNS ansatz that represents a 1D quantum state on a (1+1)-dimensional lattice of isometric tensors. One dimension corresponds to the physical spatial axis; the second, which we view as a “virtual time” axis, endows the ansatz with additional expressive power. This holographic structure enables the representation of states with volume-law entanglement, going beyond conventional ansätze with limited entanglement. Importantly, the isometric condition imposed on every tensor prevents the exponential blow-up of computational resources that would otherwise accompany this enlarged geometry. Through analytical arguments and variational benchmarks, we demonstrate that holographic isoTNS efficiently represents a broad class of physically significant wave functions characterized by high entanglement yet low complexity. Notably, fermionic Gaussian states (FGS) [31], Clifford states [32], and certain short-time-evolved states fall within this category and are represented with high fidelity by this single ansatz. Furthermore, we implement time-evolving block decimation (TEBD) algorithms for real-time evolution [21, 30]. Although the isomet-

* These authors contributed equally to this work.

ric structure ensures scalability of the algorithm, the errors accumulated during TEBD evolution limit the practical exploitation of the ansatz's high expressive power. Nevertheless, the holographic isoTNS ansatz opens a pathway toward exploration of highly entangled quantum states, advancing a frontier of quantum many-body physics beyond conventional ansätze.

The remainder of this paper is organized as follows. In Sec. II, we briefly review MPS and isoTNS in 2D, after which we formally introduce holographic isoTNS and explain their relationship to quantum circuits. In Sec. III, we closely examine the representational power of holographic isoTNS based on analytical and variational approaches. In Sec. IV, we implement the TEBD algorithm on holographic isoTNS and benchmark this method against exact time evolution. Finally, Sec. V is devoted to discussions and conclusions.

II. HOLOGRAPHIC ISOTNS

Let us begin with a general representation of a quantum many-body state. A pure state with L local degrees of freedom—such as lattice sites or particles—can be expressed as

$$|\Psi\rangle = \sum_{j_1=1}^{d_1} \sum_{j_2=1}^{d_2} \cdots \sum_{j_L=1}^{d_L} \psi^{j_1, j_2, \dots, j_L} |j_1\rangle \otimes |j_2\rangle \otimes \cdots \otimes |j_L\rangle,$$

where $\{|j_n\rangle\}$ ($j_n = 1, \dots, d_n$) spans the d_n -dimensional local Hilbert space \mathcal{H}_n of site n . The set $\{|j_1\rangle \otimes \cdots \otimes |j_L\rangle\}$ constitutes an orthonormal basis of the full Hilbert space $\mathcal{H} = \bigotimes_{n=1}^L \mathcal{H}_n$, and the complex coefficients $\psi^{j_1, j_2, \dots, j_L}$ fully specify the many-body state. In the following, we set $d_n = d$ for simplicity. Since the dimension of \mathcal{H} grows exponentially as d^L , exact treatments quickly become infeasible as L increases. Tensor network representations address this hurdle by truncating the state in a controlled way, decomposing $\psi^{j_1, j_2, \dots, j_L}$ into a network of low rank tensors.

A. Brief review of isometric MPS

MPS are a cornerstone of tensor network theory [10–12]. An MPS is defined by recasting the wave function coefficients as

$$\psi^{j_1, j_2, \dots, j_L} = \sum_{\alpha_1=1}^{\chi_1} \sum_{\alpha_2=1}^{\chi_2} \cdots \sum_{\alpha_{L-1}=1}^{\chi_{L-1}} A_{1, \alpha_1}^{[1], j_1} A_{\alpha_1, \alpha_2}^{[2], j_2} \cdots A_{\alpha_{L-1}, 1}^{[L], j_L}, \quad (1)$$

where each rank-3 tensor $A_{\alpha_{n-1}, \alpha_n}^{[n], j_n}$ has a physical index j_n that specifies a basis state on site n and two virtual indices α_{n-1} and α_n whose dimensions (i.e., bond dimensions) are χ_{n-1} and χ_n , respectively (with $\chi_0 = \chi_L = 1$). For a generic quantum state, the required bond dimension χ_n grows exponentially with the system size. Computations therefore rely on an approximate form in which every bond is truncated to a fixed maximum dimension χ . This dramatically reduces the number of parameters from exponential to linear in L . Typically, truncation is

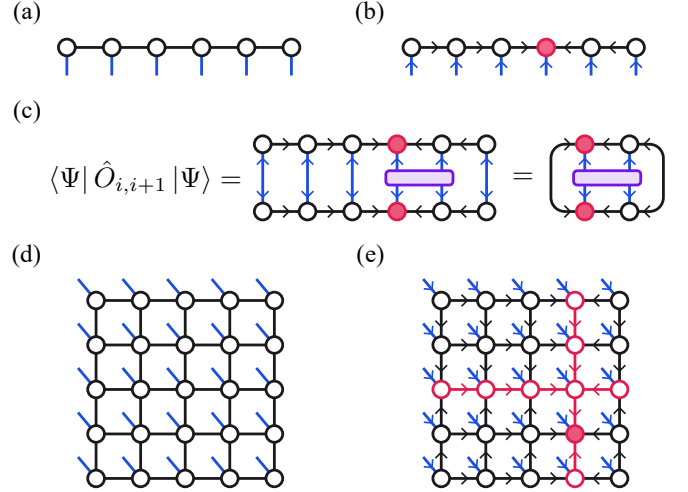


FIG. 1: Graphical notation for tensor networks. Each circle is a tensor, with blue bonds for physical legs and black bonds for virtual legs connecting the tensors. Arrows indicate isometries. (a) Generic MPS. (b) MPS in isometric form, where all tensors are isometries directed toward the orthogonality center (filled red). (c) Contraction scheme for the local two-site expectation value $\langle \Psi | \hat{O}_{i, i+1} | \Psi \rangle$. Due to the isometric form, most of the network contracts to identity, leaving a non-trivial contraction of only four tensors. (d) PEPS representing a 2D quantum state on the square lattice. (e) isoTNS for the same 2D system, where the orthogonality surface is drawn in red and the orthogonality center tensor is filled red.

carried out via singular value decompositions (SVDs) that discard the smallest Schmidt coefficients across each bond. The price paid is an upper bound on the entanglement: the entanglement entropy is upper bounded by $S \leq \log \chi$ for any bipartition, where $S = -\text{Tr} \rho_A \log \rho_A$ is the von Neumann entropy of the reduced density matrix ρ_A . Therefore, while MPS faithfully describe low entangled states, more general states with volume-law entanglement are outside the efficient reach of MPS. Nevertheless, because ground states of gapped, local Hamiltonians obey area-law scaling [8, 9], MPS have proven to be a powerful tool for exploring the low-energy physics of quantum many-body systems.

To obtain stable and fast MPS algorithms, it is advantageous to impose isometric constraints on the tensors [29, 30]. A matrix $W \in \mathbb{C}^{n \times m}$ with $n \geq m$ is an isometry if

$$W^\dagger W = \mathbb{1}_m, \quad WW^\dagger = \mathbb{P}_n, \quad (2)$$

where $\mathbb{1}_m$ is the identity on the smaller subspace and \mathbb{P}_n is a projector from the larger subspace into the smaller one ($\mathbb{P}_n^2 = \mathbb{P}_n$). When $n = p$, isometries correspond to unitaries. The definition extends naturally to higher rank tensors by grouping indices. Throughout this work we employ the usual tensor network diagram notation: tensors appear as nodes (circles) and their indices as legs; contracting two legs denotes a summation over the shared virtual index. As an example, we draw the MPS Eq. (1) in tensor diagram notation in Fig. 1a. Additionally, to visually represent isometries, we decorate the legs with arrows, pointing from the larger subspace dimension towards the smaller one. This provides a compact

diagrammatic representation of the condition in Eq. (2):

$$W = \begin{array}{c} \text{---} \\ \text{---} \\ \text{---} \end{array} = \begin{array}{c} \text{---} \\ \text{---} \\ \text{---} \end{array} =: \begin{array}{c} \text{---} \\ \text{---} \\ \text{---} \end{array}, \quad W^* = \begin{array}{c} \text{---} \\ \text{---} \\ \text{---} \end{array} = \begin{array}{c} \text{---} \\ \text{---} \\ \text{---} \end{array}.$$

By consecutively applying QR decompositions or SVDs, any MPS can be brought into its *isometric form* in Fig. 1b: a single site is selected as the orthogonality center, while every other tensor is taken to be isometric with bond arrows all directed towards the orthogonality center. It is worth emphasizing that the isometric form of MPS is exact, i.e., every MPS can be brought into isometric form without error. Shifting the orthogonality center is purely a gauge choice and can be carried out without introducing error. This isometric form is computationally advantageous in both efficiency and numerical stability. For example, when computing the norm $\langle \psi | \psi \rangle$, the isometric tensors cancel pairwise, leaving only a single contraction at the orthogonality center. An analogous simplification applies to a local expectation value $\langle \psi | O_{i,i+1} | \psi \rangle$: one first moves the orthogonality center to site i or $i+1$, after which the isometry condition can be used to reduce the computation to a contraction of only four tensors and the gate itself, as shown in Fig. 1c.

B. IsoTNS in 2D quantum systems

Tensor network representations can be extended naturally to higher dimensions. In 2D, MPS is naturally generalized to projected entangled-pair states (PEPS) [25]. As depicted in Fig. 1d, a PEPS consists of tensors arranged on a 2D lattice (here a square lattice), where each tensor possesses one physical leg and four virtual legs connecting to its neighbors [25, 26]. A key distinction from MPS is the fact that PEPS cannot in general be brought into an isometric form without error, a consequence of the closed loops inherent in higher-dimensional tensor networks. Notoriously, the cost of an exact contraction in PEPS increases exponentially with system size, meaning that the exact calculation of even local expectation values is generally intractable [25–28].

To overcome this computational barrier, isoTNS was introduced as a structured subclass of PEPS with built-in isometric constraints [21–24]. As shown in Fig. 1e, the network is constructed from a set of directed isometric tensors: the legs of bulk tensors point toward a designated row and column, which is called the orthogonality surface, and tensors on the orthogonality surface point toward a single tensor, which is called the orthogonality center. By direct analogy with MPS, expectation values of operators supported at the orthogonality center can be evaluated very efficiently because the surrounding isometries contract to identities. For example, computing the expectation value of a two-site operator at the orthogonality center requires the contraction of only five tensors including the operator itself. The isometric constraints therefore

avoid the exponential cost of generic PEPS, yielding a significant improvement in computational efficiency. The trade-off is reduced expressive power, since isoTNS form a strict subset of PEPS. Nevertheless, pioneering studies show that 2D isoTNS retain much of the expressive power of generic PEPS while greatly reducing computational overhead [21, 33, 34]. Subsequent extensions of the method cover fermionic systems [35, 36], thermal ensembles [37], infinite-strip geometries [38], three-dimensional lattices [39], and quantum circuits [40–42].

C. Holographic isoTNS

We here introduce the holographic isoTNS ansatz, which utilizes a (1+1)-dimensional array of isometrically constrained tensors to represent 1D quantum states. The word “holographic” highlights this dimensional difference, distinguishing it from conventional isoTNS where the dimensionality of the tensor network directly matches that of the quantum system (e.g., a 2D isoTNS for a 2D quantum system). We note that related holographic connections have been proposed in broader settings, for example between quantum channels and quantum circuits [43, 44].

Figure 2a illustrates the typical structures of holographic isoTNS. The horizontal axis represents the spatial dimension of the 1D system, while the emergent vertical axis is interpreted as a virtual time dimension. Let us first focus on the bottom row tensors, which feature physical legs representing a 1D quantum system of length L . Each tensor in this layer, denoted $T_{l,r,a}^j$, has one physical leg (index j) and three virtual legs that connect to adjacent tensors on the left (l), right (r), and above (a). In the bulk of the network (i.e., higher rows), tensors do not have physical legs, embodying the holographic representation of a 1D quantum state as a (1+1)-dimensional network. These bulk tensors, denoted $T_{l,r,b,a}$, possess four virtual legs connecting to neighbors on the left (l), right (r), below (b), and above (a). We adopt the convention of removing any tensor with only two nontrivial bonds (one incoming, one outgoing), as they can be absorbed into one of their neighboring tensors.

A central feature of this network is the orthogonality surface, a designated column in the spatial domain analogous to that of the 2D isoTNS (Fig. 1e). This configuration imposes a directed gauge on the tensor network; all horizontal bonds are isometrized towards the orthogonality surface. Within the orthogonality surface itself, a single tensor is chosen as the orthogonality center, and all vertical bonds are subsequently isometrized towards it. This hierarchical structure establishes a directed information flow spatially toward the orthogonality surface, so the tensors comprising the bulk and those on the orthogonality surface require different treatments. Bulk tensors, located outside the orthogonality surface, possess two incoming and two outgoing legs of a uniform dimension d ; they serve to distribute information across the spatial and virtual time domains, and no approximations (truncations) are introduced to them. As information cascades through the bulk, it

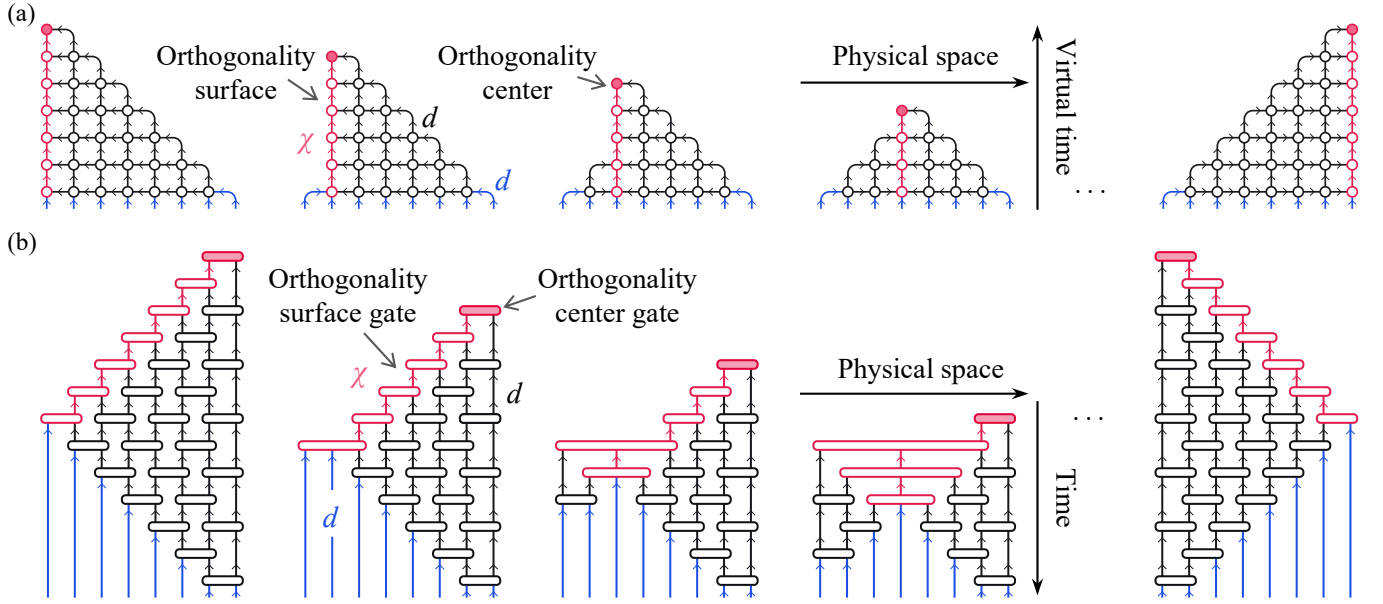


FIG. 2: (a) Diagrammatic representation of the holographic isoTNS ansatz for $L = 8$ with all possible positions of the orthogonality surface. The horizontal axis represents physical space, and the vertical axis represents the virtual time domain. Physical legs are shown in blue, and bulk tensors are colored black. The pink surface represents the orthogonality surface, with the orthogonality surface tensor highlighted as a filled circle. The bond dimension along the orthogonality surface is upper-bounded by χ , whereas all other bonds are given their full dimension of d . (b) Circuit picture of the ansatz. Each bulk tensor from (a) is mapped to a two-qudit unitary (black) acting on adjacent sites. The isometric tensors are represented by pink unitaries, which have multiple legs and act on fixed ancilla qudits [see Eq. (3)]; for clarity, we omit the ancilla qudits from this visualization, and only show one leg (corresponding to the case with $\chi = 2$). The execution time of the circuit flows in the opposite direction of the isometric arrows.

accumulates on the orthogonality surface. Consequently, the dimensions of the vertical bonds along the orthogonality surface grow exponentially and must be truncated to a maximum bond dimension χ . Standard MPS algorithms such as bond truncation and vertically shifting the orthogonality center via SVDs can directly be applied to the orthogonality surface.

These constructions give rise to the structure of holographic isoTNS shown in Fig. 2a. The architecture of the network is not fixed but is instead adaptively determined by the position of the orthogonality surface. This reflects its holographic nature: physical information is injected exclusively through the legs of the bottom tensors, while bulk tensors spanning the virtual time domain are auxiliary and possess no physical legs. Note that in conventional tensor networks such as MPS and 2D isoTNS, the network structure is fixed by the underlying lattice because all tensors are associated with physical degrees of freedom. Importantly, the isometric constraints ensure efficient tensor operations for local updates at the orthogonality surface. A key example is the calculation of a local two-site expectation value, which can be dramatically simplified as

$$\langle \Psi | \hat{O}_{i,i+1} | \Psi \rangle = \text{Diagram} = \text{Simplified Diagram},$$

where the operator $\hat{O}_{i,i+1}$ is represented as a purple gate. Anal-

ogous to contractions in an isometric form MPS (Fig. 1c), contracting any isometrized column with its complex conjugate yields the identity. This property reduces the full network evaluation to a local contraction involving only the two columns on which the operator acts. The computational cost of this contraction scales as $O(L\chi^3)$. The same simplification applies when evaluating the wave function norm $\langle \Psi | \Psi \rangle$, where the isometric constraints cancel every tensor except the orthogonality center. Normalizing the state therefore amounts to requiring that the orthogonality center be a tensor of norm one. It is worth highlighting that to leverage this efficiency for arbitrary local measurements, the orthogonality center must first be shifted to the operator's location. The systematic procedure for this shift is detailed in Sec. IV A and Appendix B.

We close by noting that a holographic isoTNS can be directly mapped onto a quantum circuit, as shown in Fig. 2b. The principle underlying this mapping is that any isometry can be extended to a unitary operator on a larger Hilbert space by incorporating ancillary degrees of freedom [40, 41, 45].

Schematically, this conversion is illustrated as

$$T_{l,r,b,a} = \text{---} = \begin{array}{c} \text{---} \\ \text{---} \\ \text{---} \\ \text{---} \\ \text{---} \end{array} = \begin{array}{c} \text{---} \\ \text{---} \\ \text{---} \\ \text{---} \\ \text{---} \end{array} = \begin{array}{c} \text{---} \\ \text{---} \\ \text{---} \\ \text{---} \\ \text{---} \end{array}, \quad (3)$$

$\chi_2 = d^m \quad d^{n+2-m}$
 $\chi_1 = d^n \quad d \quad d$

where the input and output legs with dimensions $\chi_1 = d^n$ and $\chi_2 = d^m$ are resolved into n and m qudit wires, respectively. By adjoining $n + 2 - m$ ancillary qudits, the isometry extends to a unitary gate acting on $n + 2$ qudits. The ancillary qudits are subsequently contracted with a reference state, thereby realizing the original isometry. For MPS in the isometric form (Fig. 1b), sweeping this embedding along the chain yields a unitary circuit that effectively prepares the state from ancillas initialized in a reference state. By convention, the flow of the circuit execution time is opposite to the orientation of the isometry arrows. It is worth highlighting that the representational power of quantum states generated by such tensor-network-inspired quantum circuit has been a subject of active recent study [34, 46–48].

In holographic isoTNS, the isometries on the orthogonality surface are similarly converted to unitary gates according to Eq. (3). Concurrently, the bulk isometric tensors are directly interpreted as two-qudit unitary gates, as they possess two incoming and two outgoing indices of the same bond dimension d . The composition of these two types of gates forms the full circuit representation shown in Fig. 2b, making this ansatz useful in the context of quantum computing. As in the tensor network picture, the resulting circuit architecture is determined by the location of the orthogonality surface. Placing it at the boundary produces a triangle-shaped circuit, whereas positioning it near the middle introduces intrinsically long-range isometric gates. In either case, the circuit first prepares the state by acting with isometry gates on ancilla qudits, followed by a unitary network whose depth scales as $O(L)$. The total circuit depth, corresponding to the complexity of the state [13], is therefore $O(L)$ plus the depth necessary to approximate the long-range isometric gates of the orthogonality surface by local gates [19].

III. REPRESENTATION POWER OF HOLOGRAPHIC ISOTNS

We here investigate the representational power of holographic isoTNS. By virtue of its (1+1)-dimensional structure, holographic isoTNS can plausibly reach well beyond the MPS regime. In this section, we delineate the boundary of its representable manifold through analytical constructions and variational calculations. Although no simple variational ansatz can span the entire Hilbert space, we demonstrate below that holographic isoTNS provide an efficient representation for several

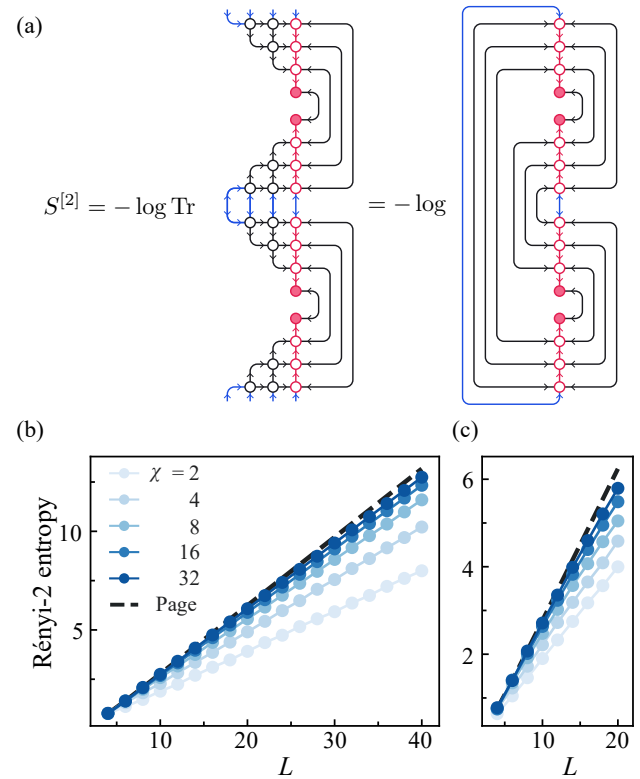


FIG. 3: (a) Contraction scheme for the calculation of the half-chain second Rényi entropy when the orthogonality surface is placed at the center of the system. (b), (c) Rényi-2 entanglement entropy $S^{[2]}$ as a function of the system size L . The blue lines represent results for holographic isoTNS with varying the bond dimension χ , and the black dashed line plots the Page value. The orthogonality surface is placed at $L/2$ for (b) and at 1 for (c). The data is averaged over 128 random realizations.

key families of quantum many-body states. In the following we set the local physical dimension $d = 2$ unless otherwise stated.

A. Entanglement volume law of typical states

First, we examine the entanglement properties of typical holographic isoTNS. We generate an ensemble of random holographic isoTNS by initializing every tensor with random coefficients drawn from the Haar distribution, subject to the required isometric constraints. For each realization, we evaluate the second Rényi entropy $S^{[2]} = -\log \text{Tr} \rho_A^2$ for a half-chain bipartition, where ρ_A is the reduced density matrix of one half of the system [49]. When the orthogonality surface is placed at the chain midpoint, the required tensor contraction reduces to the diagram shown in Fig. 3a due to the isometry conditions, which enables efficient calculation of $S^{[2]}$. Figure 3b shows the ensemble-averaged second Rényi entropy for this choice of the orthogonality surface, varying the system size L and bond dimension χ . Remarkably, the entanglement grows linearly with L in all cases. This demonstrates that typ-

ical (random) states of holographic isoTNS exhibit volume-law entanglement. Increasing the bond dimension χ results in a steeper linear growth, which systematically approaches the reference entropy for random pure states $S^{[2]} \sim (L/2-1) \log 2$, known as the Page value [50–52].

When the orthogonality surface is placed away from the midpoint ($\lfloor L/2 \rfloor$ or $\lfloor L/2 + 1 \rfloor$), the shortcut contraction of Fig. 3a is no longer applicable. For small systems, however, we can still obtain the second Rényi entropy by fully contracting the network into a 2^L -dimensional state vector and then computing $S^{[2]}$ directly. Figure 3c plots the resulting $S^{[2]}$ for randomly initialized holographic isoTNS with the orthogonality surface fixed at site 1 (leftmost). The entanglement exhibits clear volume-law scaling, similar to the results in Fig. 3b. We confirm that this volume-law behavior persists for other choices of the orthogonality surface location.

This capacity to represent extensive entanglement is an intrinsic feature of the (1+1)-dimensional architecture sketched in Fig. 2a. For a half-chain bipartition, the number of horizontal bonds cut along the spatial dimension grows linearly with the system size L . Crucially, these spatial bonds are never truncated; all truncations occur only on the orthogonality surface, where bonds run vertically in the virtual time direction. Because each untruncated spatial bond can carry entanglement, the total entanglement entropy can scale linearly with L —a volume law in 1D. This behavior contrasts sharply with MPS, where the two halves of the system are connected by a single spatial bond. Truncating that lone bond immediately and rigidly bounds the entanglement entropy, precluding any volume law growth. Therefore, the ability to capture volume-law entanglement is one of the most significant characteristics of holographic isoTNS.

B. Exactly representable classes of states

Building on the discussion of entanglement above, we now analytically and variationally demonstrate representability of holographic isoTNS for concrete families of states.

MPS. —We begin with two canonical examples: the Greenberger–Horne–Zeilinger (GHZ) state [53] and the W state [54]. Defined as $|\text{GHZ}\rangle = \frac{1}{\sqrt{2}}(|00\dots 0\rangle + |11\dots 1\rangle)$ and $|\text{W}\rangle = \frac{1}{\sqrt{L}}(|10\dots 0\rangle + |01\dots 0\rangle + \dots + |00\dots 1\rangle)$, respectively, both states have Schmidt rank 2 across any nontrivial bipartition. This allows them to be represented exactly by MPS with bond dimension $\chi = 2$. Notably, the holographic isoTNS architecture naturally accommodates such states. By setting all tensors in rows above the physical layer to identity operators, the whole network effectively reduces to 1D MPS in the bottom row with bond dimension $\chi = 2$. Consequently, holographic isoTNS can exactly represent the GHZ and W states—and indeed any state with Schmidt rank 2—irrespective of the location of the orthogonality surface.

By rotating our viewpoint by 90°, we further find that any MPS can be embedded in holographic isoTNS. Specifically, when the orthogonality surface is placed at the boundary, the target MPS tensors can be encoded vertically on the orthogonality surface, while all bulk tensors are set to the identity. Be-

cause nontrivial bulk tensors enlarge the variational space, this construction shows explicitly that holographic isoTNS with this surface position are strictly more expressive than MPS at the same bond dimension. When the orthogonality surface is positioned elsewhere, some of its tensors receive virtual indices from both horizontal directions. Geometrically, this is equivalent to folding an MPS at an intermediate point and merging the two overlapping virtual bonds of dimension χ into a single bond of dimension χ^2 . Therefore, for arbitrary placement of the orthogonality surface, holographic isoTNS with bond dimension χ^2 can exactly encode any MPS with bond dimension χ .

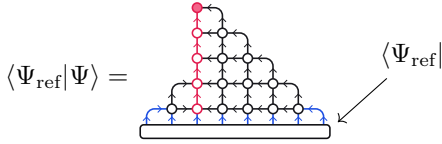
Rainbow states. —Next, beyond the area-law regime, we present an explicit construction for states with volume-law entanglement. The starting point is the circuit representation in Fig. 2b with the orthogonality surface placed at the leftmost site. By configuring a subset of the bulk gates as SWAP gates and the remainder as identity gates, we can implement an arbitrary qubit permutation $[2, 3, \dots, L-1, L] \mapsto [\sigma(2), \sigma(3), \dots, \sigma(L-1), \sigma(L)]$. Consequently, the orthogonality surface becomes equivalent to MPS whose physical indices are ordered according to the permutation $(1, \sigma(2), \sigma(3), \dots, \sigma(L-1), \sigma(L))$. For instance, this construction can generate states that are tensor products of entangled two-qubit pairs:

$$|\Psi\rangle = |\psi_2\rangle_{1,\sigma^{-1}(2)} \otimes |\psi_2\rangle_{\sigma^{-1}(3),\sigma^{-1}(4)} \otimes \dots \otimes |\psi_2\rangle_{\sigma^{-1}(L-1),\sigma^{-1}(L)}, \quad (4)$$

where σ^{-1} is the inverse permutation and L is assumed even for clarity. $|\psi_2\rangle_{i,j}$ denotes an entangled two-qubit state on qubits i and j ; for bond dimension $\chi \geq 4$, each $|\psi_2\rangle_{i,j}$ can be chosen arbitrarily. Because the permutation σ can entangle arbitrarily distant pairs of qubits, the resulting state $|\Psi\rangle$ generally exhibits volume-law entanglement. A particularly illuminating choice is the *rainbow* permutation: $\sigma(2m-1) = m$ and $\sigma(2m) = L-m+1$ for $1 \leq m \leq L/2$. This permutation pairs qubits symmetrically across the center of the chain. If each pair $|\psi_2\rangle_{i,j}$ is prepared in a maximally entangled singlet state, $|\Psi\rangle$ becomes the rainbow state, whose half-chain entanglement saturates the maximal value of $L/2 \log 2$. Note that this rainbow state appears as the ground state of the Heisenberg Hamiltonian with inhomogeneous couplings [55–57].

Variational optimization. —To assess the representational power of holographic isoTNS beyond analytic arguments, we here introduce a variational protocol. Given a reference wavefunction $|\Psi_{\text{ref}}\rangle$, we optimize all tensors in the ansatz to minimize the distance $\| |\Psi\rangle - |\Psi_{\text{ref}}\rangle \|^2$ using Riemannian variational optimization; see Appendix A for details. If the optimizer converges to the configuration that reproduces the target state within the stringent error tolerance $\| |\Psi\rangle - |\Psi_{\text{ref}}\rangle \|^2 < 10^{-14}$, we take this as positive evidence of representability of the ansatz. Conversely, failure to converge may suggest lack of representability, although this cannot be concluded definitively because the optimizer may become trapped in local minima. To minimize this possibility, we repeat each optimization with up to 1000 distinct random initializations and take the best result. When evaluating the representational power for a given class of states, exhaustive testing is infeasible. Instead, we draw 20 reference states at random from the target class and run the

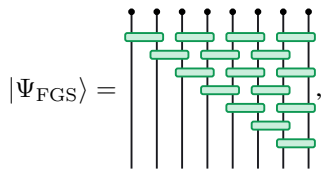
above procedure for each reference state. If the optimization finds a valid representation for every sampled instance, we regard the class as strongly supported. Note that to perform a full variational optimization, the holographic isoTNS needs to be contracted to a full state vector, e.g.,



for the computation of the overlap with a reference state $|\psi_{\text{ref}}\rangle$. This has a computational cost scaling exponential in system size, limiting the variational approach to a small number of sites.

FGS. —We first target FGS for our variational optimization. FGS appear as eigenstates of Hamiltonians quadratic in fermionic creation and annihilation operators [31]. After a Jordan-Wigner transformation, the problem moves from fermions to qubits, where each nearest-neighbor free-fermion interaction becomes a two-qubit unitary in a specific form, known as matchgates [58–61]. Consequently, a FGS can be equivalently characterized as any state prepared by a circuit of matchgates acting on a computational basis state. Note that matchgate-only circuits are not universal for quantum computation; moreover, the dynamics of FGSs are efficiently simulable on a classical computer via the covariance matrix formalism [62, 63]. In short, while FGSs may exhibit substantial entanglement, their complexity is limited by their Gaussian structure.

Based on extensive variational optimization, we find that FGSs are exactly representable by holographic isoTNS with only $\chi = 2$, independent of the location of the orthogonality surface. In particular, when the orthogonality surface is placed at the boundary, there exists a direct analytic justification via a structural correspondence. As established in Ref. [64], any matchgate circuit can be brought into a right-standard form



where the green blocks denote matchgates and the top row of dots represents the computational basis state. Strikingly, this circuit layout is structurally identical to a holographic isoTNS with its orthogonality surface at the left-most site (Fig. 2a). This allows for a one-to-one mapping: each matchgate corresponds to a gate in the same position within the holographic isoTNS circuit, and any remaining gates in the holographic isoTNS are taken to be the identity. The computational basis state naturally arises within the construction of the isometric gates [Eq. (3)], so the resulting holographic isoTNS exactly reproduces the target FGS with $\chi = 2$.

Clifford states. —We next target another prime class of highly entangled yet low complexity states: Clifford states [32]. A Clifford state is generated by the application of a Clifford circuit—composed of Hadamard, phase and CNOT

gates—to the computational basis state. On a linear nearest neighbor architecture, an arbitrary Clifford transformation can be implemented as a Clifford circuit with depth $O(7L)$, underscoring the limited complexity of this family [65, 66]. Although Clifford states admit efficient classical simulation within the stabilizer formalism, MPS are not generally efficient for this class because the states typically exhibit volume-law entanglement. We perform variational optimization for randomly generated Clifford target states using the **qiskit** [67] package with system sizes $L = 12, 13, 14$, once with the orthogonality surface at the left border and once with the orthogonality surface in the center of the chain. Remarkably, holographic isoTNS successfully represent all target states with bond dimension $\chi = 2$, strongly supporting the representability for Clifford states. Combined with results shown above, holographic isoTNS appear well-suited for states that are highly entangled yet have low complexity, which includes many states of great physical interest. Note that this is consistent with the circuit structure in Fig. 2b, whose depth effectively scales as $O(L)$ for constant χ . Such circuits can generate nontrivial entanglement but remain far shallower than the exponential depths required to produce generic high-complexity states [20].

C. Time-evolved states

An attractive application of holographic isoTNS is time evolution $|\Psi(t)\rangle = e^{-i\hat{H}t}|\Psi_0\rangle$. For a generic quantum quench in which the initial state $|\Psi_0\rangle$ is not close to an eigenstate of the Hamiltonian \hat{H} , the entanglement entropy typically grows linearly in time. This rapid entanglement growth necessitates an exponentially increasing bond dimension for accurate MPS representations, thereby limiting their use to short-time dynamics. By contrast, holographic isoTNS can efficiently represent certain volume-law entangled states, suggesting its suitability for time evolution beyond MPS. In what follows, we first assess the representational power of holographic isoTNS for time-evolved states via variational optimization; a direct simulation based on TEBD is presented in Sec. IV B.

Our first target is the Floquet dynamics of the Kicked Ising Chain (KIC) [68, 69]

$$\begin{aligned} \hat{H}_{\text{KIC}} &= \sum_{j=1}^L \left[J\hat{\sigma}_j^z\hat{\sigma}_{j+1}^z + (g\hat{\sigma}_j^x + h\hat{\sigma}_j^z) \sum_{m=-\infty}^{m=\infty} \delta(t-m) \right] \\ &\equiv \hat{H}_{\text{I}} + \hat{H}_{\text{K}} \sum_{m=-\infty}^{m=\infty} \delta(t-m), \end{aligned}$$

with $L = 14$ and $(J, g, h) = (\pi/4, \pi/4, 0.5)$. Setting the time between kicks to unity, the time evolution is given by $|\Psi(t+1)\rangle = e^{-i\hat{H}_{\text{K}}} e^{-i\hat{H}_{\text{I}}} |\Psi(t)\rangle$. We start the evolution from the fully polarized product state $|\Psi_0\rangle = |\uparrow\uparrow\dots\uparrow\rangle$. Our goal is to assess how well $|\Psi(t)\rangle$ can be represented by MPS and by holographic isoTNS. To this end, we first obtain the exact dynamics via exact diagonalization (ED), yielding a reference state $|\Psi_{\text{ref}}(t)\rangle$ at each time step t . We then variationally optimize the tensors of both ansätze to maximize the overlap

with $|\Psi_{\text{ref}}(t)\rangle$ at every time step. For these variational calculations, we place the orthogonality surface at the leftmost site. Rényi-2 entropies and variational errors are computed by exact contraction of the optimized tensor networks. Note that we choose the model parameters such that the KIC cannot be mapped to a fermionic Gaussian model, as would be the case for $h = 0$. Consequently, although time evolving a FGS with a fermionic Gaussian model results in another FGS—making it exactly representable by holographic isoTNS as discussed in Sec. III B—this does not hold for the model investigated here.

Figure 4a compares the variational performance of MPS and holographic isoTNS in representing time-evolved states of the KIC. We plot both the Rényi-2 entropy $S^{[2]}$ and the variational error $\|\langle \Psi \rangle - \langle \Psi_{\text{ref}} \rangle\|^2$ as a function of the target evolution time. The Floquet driving protocol of the KIC induces a rapid, linear growth of entanglement. Initially, the MPS ansatz faithfully reproduces the exact dynamics; however, its accuracy deteriorates abruptly once the system's entanglement approaches the maximum value sustainable by the chosen bond dimension χ . This breakdown is signaled by a distinct plateau in the calculated $S^{[2]}$ and a sharp increase in the variational error. Increasing χ extends the reliable simulation time but does not remove this limitation caused by entanglement. In contrast, the holographic isoTNS tracks the entanglement growth accurately even with small bond dimensions, demonstrating a clear advantage for highly entangled states and, consequently, for real-time quantum dynamics. Nevertheless, at longer times, the holographic isoTNS also fails to reproduce the exact state: while $S^{[2]}$ remains close to the exact value, the variational error eventually rises to a level comparable to that of MPS, albeit with a longer breakdown time for the same χ . This contrasting behavior suggests a fundamental difference between the limitations of the two ansätze. For MPS, the primary bottleneck is clearly entanglement growth. For the holographic isoTNS, which is capable of accommodating high entanglement, the failure likely reflects a different obstruction. Because unitary dynamics generically increases not only entanglement but also state complexity [19, 20], it is natural to attribute the dominant factor limiting the variational power of holographic isoTNS to the growth of complexity rather than entanglement.

To distinguish the roles of entanglement and complexity in the variational performance of our ansatz, we investigate a scenario in which the initial state already exhibits volume-law entanglement. Unlike evolution from a product state, where both entanglement and complexity increase with time (Fig. 4a), the present protocol primarily increases the state complexity while keeping the entanglement growth moderate. We construct $|\Psi_0\rangle$ as a product of long-range two-qubit states [Eq. (4)] arranged in the rainbow pairing that connects site i to site $L - (i - 1)$. Each pair is prepared in the state $|\psi_2\rangle = \sqrt{1/5}|00\rangle + \sqrt{2/5}(|01\rangle + |10\rangle)$. This construction ensures that the half-chain entanglement of $|\Psi_0\rangle$ is extensive; it scales as $L/2$ times that of $|\psi_2\rangle$. As shown in Sec. III B, $|\Psi_0\rangle$ admits an exact representation as a holographic isoTNS with $\chi \geq 4$; by contrast, it is neither a FGS nor efficiently representable as an MPS with small bond dimension. The subsequent time evolution is governed by the critical transverse-

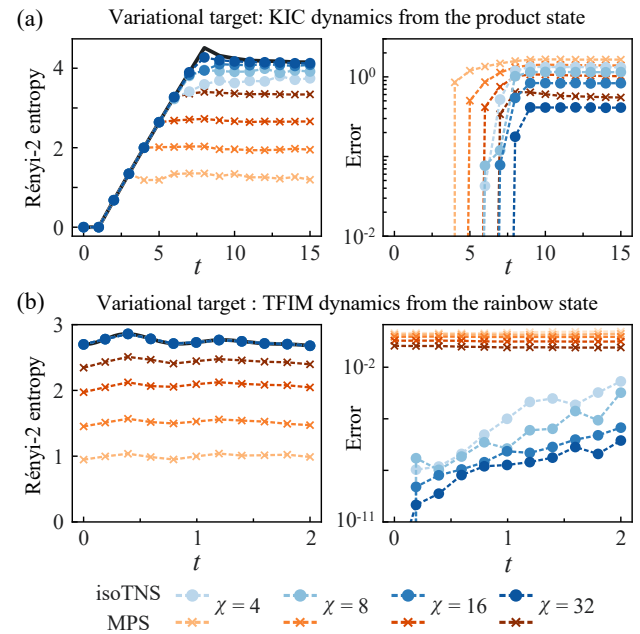


FIG. 4: Variational optimization of holographic isoTNS (blue) and MPS (red) while changing the bond dimension χ (system size $L = 14$). The left and right panels show, respectively, the Rényi-2 entropy $S^{[2]}$ and the variational error $\|\langle \Psi \rangle - \langle \Psi_{\text{ref}} \rangle\|^2$ as a function of time. (a) Dynamics under the KIC Hamiltonian at $(J, g, h) = (\pi/4, \pi/4, 0.5)$ from the product state $|\Psi_0\rangle = |\uparrow\uparrow \dots \uparrow\rangle$. (b) TFIM dynamics at $(J, g) = (1, 1)$ from the highly entangled volume-law rainbow state defined in Eq. (4). For completeness, we note that our results provide only an upper bound on the true variational error, as this computationally hard constrained optimization problem yields only local minima of the cost function.

field Ising model (TFIM):

$$\hat{\mathcal{H}} = -J \sum_i \hat{\sigma}_i^z \hat{\sigma}_{i+1}^z - g \sum_i \hat{\sigma}_i^x, \quad (J, g) = (1, 1). \quad (5)$$

A comparison with the direct real-time evolution without a global variational optimization is left to Sec. IV B.

The results of the variational simulation are summarized in Fig. 4b. Because the initial state exhibits volume-law entanglement, an MPS cannot provide a faithful representation even at $t = 0$, without an exponentially large bond dimension. In contrast, the holographic isoTNS accommodates this structure with a modest bond dimension χ and maintains a small variational error at short times. This error nevertheless grows steadily with time as the state evolves beyond the manifold representable by our ansatz. Notably, the entanglement entropy changes little during this evolution. We therefore conclude that the loss of representability during time evolution is driven by the increase of state complexity rather than by entanglement growth.

IV. SCALABLE QUANTUM SIMULATIONS

The previous section showed that holographic isoTNS can represent states ranging from area-law to certain volume-law classes, including MPS, FGS, Clifford, and short-time-evolved states. Here we shift focus from analytical and variational evaluations to scalable algorithms for quantum simulation with holographic isoTNS.

A. TEBD algorithm

We employ the TEBD algorithm for real-time evolution [30]. The overall workflow is shown in Fig. 5: nearest-neighbor two-qubit gates are applied sequentially, while the orthogonality surface is continually shifted to one of the two sites on which each gate acts. Note that this shift is introduced purely for computational convenience, allowing full exploitation of the isometric constraints during gate application.

Ideally, shifting the orthogonality surface from position i to $i + 1$ should leave the many-body state unchanged. However, for a finite χ , a holographic isoTNS with its surface at one site cannot, in general, be exactly represented by one with the surface at another site. This discrepancy arises because the effect of truncations is dependent on the surface position. Nevertheless, there is no *a priori* physical reason to expect that accurate state representations should exist for only a restricted set of orthogonality surface positions. We therefore posit that for physically relevant states, the choice of surface location has only a minor quantitative effect on the approximation error, which should decrease as χ increases. This assumption justifies shifting the orthogonality surface as needed to optimize computational efficiency.

For a given state $|\Psi_{\text{before}}\rangle$ with the orthogonality surface at i , we calculate the post-shift state as the solution of the variational problem $|\Psi_{\text{after}}\rangle = \text{argmin}_{|\Psi'\rangle} \|\Psi_{\text{before}}\rangle - |\Psi'\rangle\|^2$, where $|\Psi'\rangle$ is constrained to be a holographic isoTNS with its orthogonality surface at $i + 1$. In principle, attaining the optimum requires optimization over all tensors, but the associated cost is exponential. Instead, we optimize only the tensors in columns i and $i + 1$, keeping all others fixed. This is a reasonable approach because the shift alters the network structure only at these columns [see Fig. 2a]. By virtue of the isometric constraints of tensors remaining unchanged by the shift, the variational problem reduces to minimizing the distance between the two affected columns, $T_{\text{after}}^{[i,i+1]} = \text{argmin}_{T'} \|T_{\text{before}}^{[i,i+1]} - T'\|$, where $T_{\text{before}}^{[i,i+1]}$ denotes the tensors in columns i and $i + 1$ of $|\Psi_{\text{before}}\rangle$ (after). We optimize the tensors in these columns using an alternating linear optimization scheme [70, 71]; see Appendix A. The approximate shift of the orthogonality surface is diagrammatically represented as

$$\begin{array}{c} \text{Diagram 1} \\ \approx \\ \text{Diagram 2} \end{array} \quad (6)$$

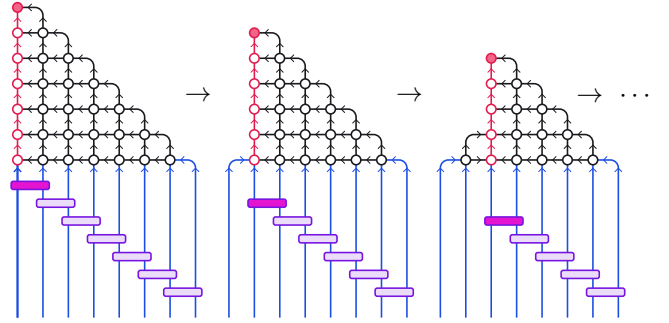


FIG. 5: The TEBD algorithm on holographic isoTNS. The time-evolution operator is approximated via the 1st-order Suzuki-Trotter decomposition into nearest-neighbor gates. Gates are applied in a left-to-right sweep at odd time steps; for even time steps, a right-to-left sweep is performed (only odd time steps are shown). At each gate application, the orthogonality surface is shifted accordingly to one of the sites where the gate is applied.

Notably, this procedure can be carried out systematically using the “Moses move” algorithm [21, 34] (see Appendix B for implementation details). In practice, we use the Moses move output as an initial guess for a subsequent alternating linearized optimization that further refines the solution [34]. It is important to note that, since shifting the orthogonality surface generally introduces some error, it is crucial to minimize the number of necessary shifts in any algorithm on holographic isoTNS.

For a given Hamiltonian, the TEBD algorithm advances the state by applying the time evolution operator $U(\Delta t) = e^{-i\mathcal{H}\Delta t}$ over a small time step Δt . A first-order Suzuki-Trotter decomposition approximates $U(\Delta t)$ as a product of nearest-neighbor two-site gates,

$$U(\Delta t) = \prod_{i=1}^{N-1} U^{[i,i+1]}(\Delta t) + O(\Delta t^2),$$

where $U^{[i,i+1]}(\Delta t)$ acts locally on sites i and $i + 1$. Figure 5 illustrates the gate-application sequence for an odd time step, in which the gates are applied successively from the leftmost bond to the rightmost; for an even time step, they are applied in the reverse order, from the right to the left. This alternating ordering minimizes the number of required shifts of the orthogonality surface within each time step. It is worth noting that decreasing Δt or using a higher-order decomposition reduces the Trotter error, but it requires additional shifts of the orthogonality surface, which increases the cumulative error in the full simulation.

The gate application is formulated as a variational problem. Given a holographic isoTNS $|\Psi\rangle$ and a unitary gate $U^{[i,i+1]}$, we search for an updated holographic isoTNS of identical structure $|\Phi\rangle$ that best approximates the evolved state: $\text{argmin}_{|\Phi\rangle} \|\Phi\rangle - U^{[i,i+1]}|\Psi\rangle\|^2$. Because $U^{[i,i+1]}$ acts only on sites i and $i + 1$, we assume that tensors outside the i - and $(i+1)$ -th columns remain unchanged. Under the isometric constraints imposed on these uninvolved tensors, the optimization problem reduces to $\text{argmin}_{T_{\Phi}^{[i,i+1]}} \|T_{\Phi}^{[i,i+1]} - U^{[i,i+1]} T_{\Psi}^{[i,i+1]}\|$, where

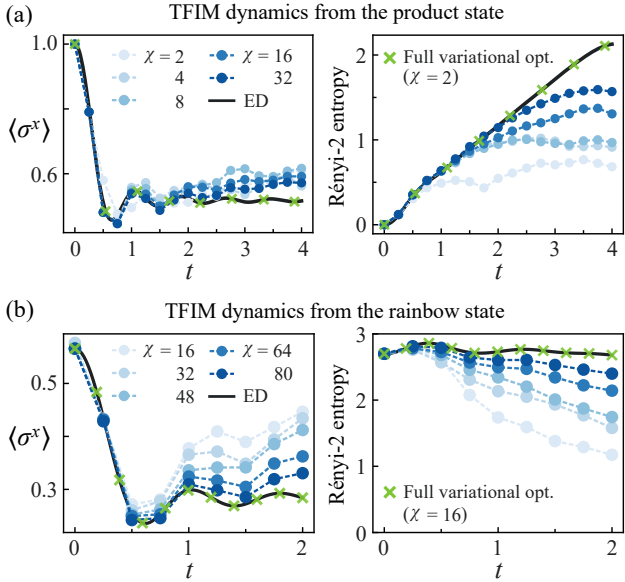


FIG. 6: (a) Time evolution of the mean value of $\langle \sigma^x \rangle$ (left) and the Rényi-2-entropy $S^{[2]}$ (right) using the TEBD algorithm. The evolution is calculated under the TFIM Hamiltonian at $(J, g) = (1, 1)$ in Eq. (5) with the system size $L = 14$. The initial state is prepared in a product state $|++\cdots++\rangle$; the time evolution keeps the states as FGS, and thus they should be exactly represented by our ansatz. (b) The same plot as (a), starting from the volume-law rainbow state in Eq. (4). Variational optimization results [see Fig. 4(b)] suggest that it can be approximated well by holographic isoTNS. In both panels, the blue lines show the evolution of holographic isoTNS using TEBD with varying bond dimension χ , while the black curve indicates the ED results. For comparison, the results from full variational optimization with $\chi = 2$ in (a) and $\chi = 16$ in (b) are shown as green markers, which overlap with the black curves. The time discretization for a single TEBD step is set as $\Delta t = 0.25$.

$T_{\Phi}^{[i,i+1]}$ denotes the tensors on the i -th and $(i+1)$ -th columns of $|\Phi\rangle\langle\Psi\rangle$. Since $U(\Delta t)$ is close to the identity for small Δt , the pre-gate tensors $T_{\Phi}^{[i,i+1]}$ provide a good initial guess for the post-gate tensors $T_{\Psi}^{[i,i+1]}$, which is then refined through an iterative alternating optimization, see Appendix A. Repeating this procedure for every gate at each time step following Fig. 5 produces the full TEBD evolution of holographic isoTNS.

B. Real-time evolution

We benchmark the performance of the TEBD algorithm by simulating real-time evolution under the critical TFIM Hamiltonian [Eq. (5)]. We consider two distinct initial states: (i) the fully polarized product state $|++\cdots++\rangle$ and (ii) the volume-law entangled rainbow state of Eq. (4), with the same parameter as in Fig. 4b. The representational power of holographic isoTNS for these dynamics is already established in previous sections. In case (i), the initial state is a FGS, and because the Hamiltonian is quadratic in its fermionic representation [72],

the evolved states remain FGS [31]. Hence, the full time evolution can be captured already with $\chi = 2$ given the exact representability of FGS discussed in Sec. III B. In case (ii), we have shown variationally that holographic isoTNS reproduces short-time behavior accurately, whereas an MPS fails already at $t = 0$ (Fig. 4b). Consequently, the present benchmarks primarily probe the effectiveness of the TEBD algorithm rather than the expressivity of the ansatz.

Figure 6a shows the TEBD results for the spatially averaged magnetization $\langle \sigma^x(t) \rangle = \sum_{i=1}^L \langle \sigma_i^x(t) \rangle / L$ and the Rényi-2-entropy $S^{[2]}(t)$ and compares them against ED results. We also show the results from variational optimization in green markers. Notably, despite the known representability for FGS time evolution, both $\langle \sigma^x(t) \rangle$ and $S^{[2]}(t)$ agree with the ED results only up to $t < 2$ for our largest $\chi = 32$; beyond this, the TEBD simulation no longer tracks the exact dynamics, with discrepancies increasing for smaller χ . For reference, we confirm that an MPS with $\chi = 32$ faithfully reproduces the dynamics over the time window considered. We attribute this breakdown of holographic isoTNS to the repeated shifts of the orthogonality surface inherent to the TEBD. Our working assumption is that physically relevant states that are representable for one surface location remain representable for other locations. If this condition fails, TEBD necessarily breaks down, whereas it is strongly suggested to hold for FGS due to its exact representability. Nevertheless, even when the target state lies in the overlap of such manifolds, moving between them may require a global reoptimization of all tensors, and the local update in Eq. (6) does not guarantee a successful transition. Consequently, repeated shifts can gradually drive the state away from the exact time evolution even for FGS. This interpretation is supported by the observation that decreasing the Trotter step Δt worsens the agreement—despite smaller Trotter errors—because it increases the number of orthogonality surface shifts, which we find to be detrimental.

Figure 6b displays the TEBD dynamics initialized from the highly entangled rainbow state. We verified variationally that holographic isoTNS can closely represent the corresponding evolved states, as shown in green markers. The simulation indeed faithfully captures the short-time regime (e.g., for $t \leq 0.75$ with $\chi = 80$), which is inherently non-accessible to MPS. However, as in Fig. 6a, deviations from the ED result emerge at later times. Most notably, $S^{[2]}$ decreases from its initially large value even at high bond dimensions, indicating that shifts of the orthogonality surface spuriously reduce entanglement and thereby undermine the primary strength of holographic isoTNS.

These benchmarks reveal a fundamental algorithmic limitation of the current holographic isoTNS optimization. Although the ansatz itself has substantial representational power, our present TEBD implementation (Sec. IV A) cannot fully exploit it. The core bottleneck is the shifting orthogonality surface: to keep the algorithm scalable, we restrict updates to local tensors, which can introduce errors from inconsistencies between the pre- and post-shift states. More global update schemes could mitigate this, but they incur exponential cost per TEBD step, which runs counter to our original motivation for imposing isometric constraints to avoid exponentially

expensive contractions. Designing a scalable algorithm that fully leverages the variational power of holographic isoTNS therefore remains a significant open challenge.

V. CONCLUSIONS

In conclusion, we introduced holographic isoTNS to represent highly entangled 1D many-body quantum states. Our ansatz is a (1+1)-dimensional network in which one axis represents real space while the other, a virtual time axis, substantially enhances expressive power. All tensors are isometrized toward the orthogonality surface and, within that surface, toward the orthogonality center. Therefore, contractions involving the orthogonality center remain efficient even in the enlarged network—consistent with the philosophy of isoTNS. When randomly initialized, holographic isoTNS realizes volume-law entangled states, evidencing expressivity beyond both MPS and TTN. Through analytic arguments and variational studies, we further show that several important classes, such as MPS, FGS, and Clifford states, are naturally captured within our ansatz. The latter two exemplify systems with substantial entanglement yet modest circuit complexity. Moreover, our variational analysis of time-evolved states reveals that increasing complexity, rather than entanglement, is the principal limiting factor for representation of long-time-evolved states. We therefore conclude that holographic isoTNS is particularly well suited to highly entangled, low-complexity states—a regime encompassing many physically relevant situations—suggesting broad impact for quantum many-body studies. To exploit this capacity, we further implemented a TEBD scheme tailored to the ansatz with a computational cost scaling quadratically in system size. However, we found that errors accumulated over TEBD sweeps quickly lead to deviations from exact dynamics. Designing scalable algorithms that preserve this efficiency while controlling error growth remains a compelling direction for future work.

Several generalizations of holographic isoTNS can be made. For two spatial dimensions, a (2+1)-dimensional holographic isoTNS on a cubic lattice would naturally represent volume-law entangled states in 2D many-body systems, providing a platform to probe nontrivial topology and long-range entanglement [39]. Infinite systems with translational invariance offer another compelling arena. In this setting one would construct the state by applying a finite number of layers of unitary tensors to an infinite MPS with a given unit cell, each of the layers consisting of a repeated unit cell of unitaries. To move the orthogonality surface one would have to devise a version of the Moses move for an infinite system, where the infinite direction is orthogonal to the orthogonality surface [38]. Extensions to fermionic degrees of freedom are likewise promising [35, 36]. In 1D, the Jordan-Wigner transformation maps fermions to qubits; although it introduces nonlocal strings, these do not pose a major obstacle for our ansatz, which is designed to capture large entanglement. In higher dimensions, however, faithfully encoding fermionic anticommutation within the holographic structure is nontrivial

and remains an open direction. Overall, we emphasize that the existing body of work on isoTNS provides strong guidance for these extensions of holographic isoTNS.

The quantum circuit viewpoint suggests a complementary route to extending holographic isoTNS [40]. Because the isometric constraints impose a directed flow of information, the network admits a natural mapping to a quantum circuit. Such quantum circuit ansätze are known to be highly expressive despite their sparsity, as demonstrated by numerous recent works [19, 46, 47]. This perspective motivates an inverse construction: Using a given quantum circuit ansatz as a blueprint to define an alternative holographic isoTNS structure that encodes it. In particular, circuits with nonlocal gates, multi-qudit gates, or mid-circuit measurements could be embedded naturally within an extended holographic isoTNS. The notion of an orthogonality surface can then be modified more flexibly, potentially enabling error-free orthogonality surface shifts. The richer geometries they would support better embody the holographic concept, in which the virtual time axis is decoupled from the physical degrees of freedom. Systematically exploring holographic isoTNS configurations in tandem with quantum circuit ansätze is therefore a promising direction for future work.

ACKNOWLEDGMENTS

The authors thank Sheng-Hsuan Lin, Sajant Anand, Raúl Morral-Yepes, Marc Langer, Bernhard Jobst, Masataka Kawano, Johannes Hauschild and Yukitoshi Motome for fruitful discussions. We particularly thank Michael P Zaletel for discussions and related collaborations. K.K. was supported by the Program for Leading Graduate Schools (MERIT-WINGS) and JST BOOST (No. JPMJBS2418). This work was supported by the European Research Council (ERC) under the European Union’s Horizon 2020 research and innovation program under Grant Agreements No. 771537 and No. 851161, the Deutsche Forschungsgemeinschaft (DFG, German Research Foundation) under Germany’s Excellence Strategy EXC-2111-390814868, TRR360-492547816, and the Munich Quantum Valley, which is supported by the Bavarian state government with funds from the Hightech Agenda Bayern Plus.

Data and materials availability. Data analysis and simulation codes are available on Zenodo upon reasonable request [73].

Appendix A: Variational Optimization of holographic isoTNS

In the following we show how one can optimize a holographic isoTNS to minimize a given cost function. We start by defining the problem as a general optimization problem, and proceed to give details on two specific methods to solve the problem. Consider the cost function

$$f : \mathbb{C}^{n_1 \times m_1} \times \mathbb{C}^{n_2 \times m_2} \times \cdots \times \mathbb{C}^{n_N \times m_N} \times \mathbb{C}^p \rightarrow \mathbb{R},$$

mapping $N+1$ tensors to a scalar cost value. This cost function can, for instance, represent the contraction of a tensor network consisting of N isometric tensors $W_i \in \mathbb{C}^{n_i \times m_i}$ with $n_i \geq m_i$ and (optionally) an orthogonality center tensor $T \in \mathbb{C}^p$, where we have reshaped the isometric tensors into isometric matrices and the orthogonality center into a vector. Examples for such cost functions f are the overlap of a holographic isoTNS with a reference wavefunction $\langle \Psi_{\text{isoTNS}} | \Psi_{\text{ref}} \rangle$ or the energy $\langle \Psi_{\text{isoTNS}} | \hat{\mathcal{H}} | \Psi_{\text{isoTNS}} \rangle$ of a holographic isoTNS for a model Hamiltonian $\hat{\mathcal{H}}$. We are interested in the constrained optimization problem

$$W_1^{\text{opt}}, W_2^{\text{opt}}, \dots, W_N^{\text{opt}}, T^{\text{opt}} = \underset{W_1, W_2, \dots, W_N, T}{\text{argmax}} \quad f(W_1, W_2, \dots, W_N, T)$$

under the constraints $W_i^\dagger W_i = \mathbb{1}$ for isometries and $\|T\| = 1$ for the orthogonality center. In the following we discuss two methods for solving this optimization problem, namely an alternating linearized optimization scheme due to Evenbly and Vidal [70, 71], and Riemannian optimization of product manifolds.

1. Alternating linearized optimization

Assume first that the cost function is linear in all its arguments, i.e., given by the contraction of a tensor network in which each tensor appears only once. In this case, one can extremize the cost function by iteratively optimizing one tensor at a time. To optimize an isometry $W_i \in \mathbb{C}^{n_i \times m_i}$, we first contract the tensor network without W_i into an environment tensor $E \in \mathbb{C}^{n_i \times m_i}$. The optimal tensor W'_i when keeping all other tensors fixed is then given by

$$W'_i = \underset{W_i^\dagger W_i = \mathbb{1}}{\text{argmax}} \text{Tr}(W_i^\dagger E).$$

This optimization problem is known as the *orthogonal Procrustes problem* and permits the closed form solution

$$W'_i = U V^\dagger, \quad (\text{A1})$$

where the matrices U and V are defined through the SVD $E = U S V^\dagger$. Similarly, if the tensor to be optimized is the orthogonality center T , contracting all other tensors into an environment $E \in \mathbb{C}^p$ yields the optimization problem

$$T' = \underset{\|T\|=1}{\text{argmax}} \text{Tr}(T^\dagger E),$$

which is solved by

$$T' = E / \|E\|.$$

For derivations of the closed form solutions, see the appendices of Refs. [24, 34].

Each of these local updates is optimal and thus the value of the cost function is never decreased. Therefore, If the cost function is linear in all tensors and bounded, $f(W_1, \dots, W_N, T) \leq c \in \mathbb{R}$, the algorithm is guaranteed to converge to a local maximum.

In general the cost function f is not linear. Non-linear cost functions are for example encountered when optimizing a MERA wavefunction or during the disentangling step in the Moses move (see Appendix B). Assume that the tensor W_i appears more than once in the tensor network describing the cost function. It was proposed by Evenbly and Vidal [70, 71] in the context of MERA to linearize the cost function and to update the tensor W_i iteratively such that the linearized cost function is minimized in each iteration. For this, we contract all tensors except one of the tensors W_i into an environment $E(W_i) \in \mathbb{C}^{n_i \times m_i}$, which now depends on W_i . We then update W_i by treating the environment as if it were independent of W_i and employing the closed form update Eq. (A1). This is repeated until W_i is converged. However, if and how fast W_i converges depends on the cost function, and convergence cannot be guaranteed in general.

2. Riemannian Optimization

The alternating linearized optimization can only be used if the cost functions can be expressed as the contraction of a tensor network. Additionally, the method often converges only very slowly, especially if the cost function depends on many tensors. Riemannian optimization generalizes known euclidean optimization algorithms like Gradient Descent, Conjugate Gradients (CG) and quasi-newton methods like the Trust Region Method (TRM) to *Riemannian manifolds*. In the following, we give a brief introduction to Riemannian optimization. For an in-depth introduction to the topic we recommend Refs. [74–76].

Let us first assume that the cost function depends only on a single tensor, which can either be constrained to be an isometry or a tensor of norm one. The space of all $n \times m$ isometries W is a Riemannian manifold called the *Stiefel manifold* $\text{St}(n, m)$. Likewise, the complex unit sphere $S^{2p-1} \subset \mathbb{C}^p$, i.e., the space of all vectors $T \in \mathbb{C}^p$ of norm one, $\|T\| = 1$, is a Riemannian manifold. In the following, let \mathcal{M} denote the manifold which we want to optimize over. Standard optimization algorithms iteratively improve an iterate $X_k \in \mathcal{M}$, $k = 1, 2, \dots$ until a local extremum of the cost function $f : \mathcal{M} \rightarrow \mathbb{R}$ is reached. At each step, the iterate is moved along an update direction ξ_k with a step size α_k . The update direction and step size are typically computed from the current and past gradients $\nabla f(X_k)$ and sometimes higher derivatives of the cost function. In optimization algorithms defined on Euclidean vector spaces, the update direction lies in the same vector space as the iterates X_k , and the iterate can simply be updated as $X_{k+1} = X_k + \alpha_k \cdot \xi_k$. When optimizing over a Riemannian manifold, the update direction should first be projected into the tangent space $T_{X_k} \mathcal{M}$ to the manifold \mathcal{M} at point $X_k \in \mathcal{M}$ [74]. Further, just updating the iterate by moving the current iterate along the update direction would in general leave the manifold. To ensure that we stay on the manifold, $X_{k+1} \in \mathcal{M}$, one can introduce a *retraction* $R_{\xi_k} : \mathbb{R} \rightarrow \mathcal{M}$. One can think of $R_{\xi_k}(\alpha_k)$ as moving along the direction of ξ_k , starting from X_k , with a step size of α_k , while staying on the manifold \mathcal{M} . A practical retraction for the Stiefel manifold is given

by $R_{\xi_k}(\alpha_k) = \text{qf}(X_k + \alpha_k \xi_k)$ [74], where $\text{qf}(A)$ denotes the Q -factor of the QR-decomposition $A = QR$. For the complex unit sphere, the contraction $R(\xi_k) = (X_k + \alpha_k \xi_k)/\|X_k + \alpha_k \xi_k\|$ can be used [74].

Some algorithms, e.g. CG, need gradients of the cost functions at previous iterates for computing the update direction at the current iterate. Since the tangent spaces at two iterates X_k and $X_{k'}$ are generally different, previous gradients need to first be brought to the tangent space of the current iterate using a *vector transport* $T_{k \rightarrow k'} : T_{X_k} \mathcal{M} \rightarrow T_{X_{k'}} \mathcal{M}$ [74]. A particularly simple vector transport for the Stiefel manifold and the complex unit sphere can be implemented by simply projecting gradients at previous iterates to the tangent space of the current iterate. Lastly, second order algorithms such as the TRM require the generalization of the Hessian-vector product to Riemannian manifolds, which is given by the *Riemannian connection*. For the Stiefel manifold (the complex sphere), the Hessian-vector product can be computed by projecting the Hessian-vector product from the embedding vector space $\mathbb{C}^{n \times m}$ (\mathbb{C}^p) to the manifold.

In this work, we used two optimization algorithms, CG and the TRM. CG uses accumulated gradients from previous iterates to compute improved orthogonal search directions. The TRM locally approximates the cost function using a quadratic model within a neighborhood of radius Δ_k around the current iterate X_k . This approximate model is then minimized inside the trust region using truncated Conjugate Gradients (tCG), which is particularly efficient for quadratic problems. Based on how well the model approximates the true cost function at the current iterate, the trust region can be either expanded or contracted. The TRM combines the advantages of local super-linear convergence with certain global convergence guarantees [74], and can be viewed as an enhanced version of Newton's method. For a more in-depth discussion of CG and the TRM, see Refs. [74, 76–79]. In this work, we use the CG and TRM algorithms implemented in the **pymanopt** package [79]. Gradients and higher order derivatives are computed using the **autograd** feature in **jax** [80].

Appendix B: Moses move

As emphasized in the main text, the strength of holographic isoTNS stems from efficient contraction outside the orthogonality surface by virtue of the isometric conditions. Hence, shifting the orthogonality surface is of fundamental importance for our ansatz. The Moses move provides a systematic prescription for this shift [21, 34]. The core step of the Moses move is a tripartite tensor decomposition of the orthogonality center tensor, sketched in Fig. 7a. We denote the tensor to be decomposed by $T_{l,b,a,r,\alpha}$ with subscripts labeling the left, below, above, and right legs, and the down-right ancillary leg, respectively. A detailed account of the meaning of these legs is postponed until after the full procedure has been outlined; for the moment we assume that the left, right, and below legs have bond dimension 1 or d , while those of the above and ancillary legs are bounded by χ .

The tripartite decomposition begins with a QR decomposi-

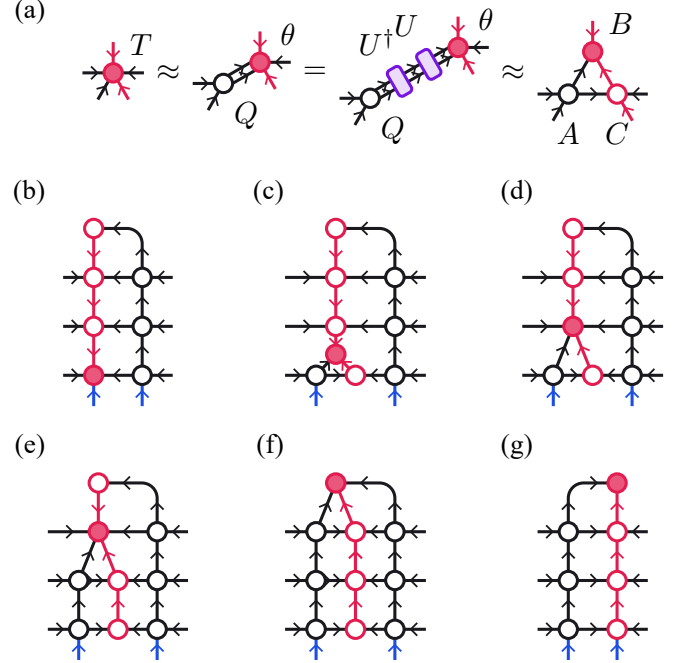


FIG. 7: A sketch of the Moses move algorithm. (a) The tripartite decomposition, as defined in Eq. (B1). (b)-(g) Steps for shifting the orthogonality surface one column to the right. (b) Initially, the orthogonality surface is on the left column. (c)-(f) The tripartite decomposition is repeatedly applied to unzip the column. (g) The intermediate column is contracted into the right column, completing the shift of the orthogonality surface.

tion of the bipartition $T_{(l,b),(a,r,\alpha)} = Q_{(l,b),\beta} \theta_{\beta,(a,r,\alpha)}$. Here Q is an isometry, and the outgoing leg β has the smaller dimension of the two grouped subspaces (l, b) and (a, r, α) ; hence $\dim \beta = 1, d$ or d^2 under the assumption introduced above. We focus on the latter two cases and further split β into two indices, β_u and β_r : when $\dim \beta = d^2$ we set $\dim \beta_u = d$ and $\dim \beta_r = d$, whereas for $\dim \beta = d$ we take $\dim \beta_u = 1$ and $\dim \beta_r = d$. Importantly, at this stage a unitary U can be inserted as a gauge degree of freedom: $T = (QU^\dagger)(U\theta) \equiv A\theta'$. A suitable choice of the disentangling unitary U redistributes the singular values and can substantially reduce the truncation error introduced in the next step. We then apply an SVD to the disentangled tensor $\theta'_{(\beta_u,a),(\beta_r,r,\alpha)} \simeq B_{(\beta_u,a),\gamma} C_{\gamma,(\beta_r,r,\alpha)}$, where C is an isometry and the bond dimension of γ is truncated to the largest χ singular values. Collecting these factors yields the tripartite decomposition shown in Fig. 7a,

$$T_{l,b,a,r,\alpha} \simeq A_{l,b,\beta_u,\beta_r} B_{\beta_u,a,\gamma} C_{\gamma,\beta_r,r,\alpha}. \quad (\text{B1})$$

The accuracy of the decomposition depends sensitively on the disentangling unitary. Following Ref. [34], we select the unitary that minimizes the Rényi-1/2 entropy of the bipartition of θ' using a Riemannian-manifold optimization method. Because Rényi- n entropy with $n < 1$ bounds the truncation error at a fixed bond dimension, this criterion provides an effective means of reducing the loss of accuracy [8].

We are now ready to detail the Moses move protocol. For later reference, let $\{\Psi^{[l]}\}$ denote the tensors on the orthogonal-

ity surface column and $\{\Phi^{[h]}\}$ those in the neighboring right column, where the position label h is counted upward from the bottom. The first step shifts the orthogonality center to the bottom tensor $\Psi^{[h=1]}$; this is an exact gauge transformation that introduces no error (Fig. 7b). We then rewrite $\Psi^{[h=1]}$ as a five-leg tensor $T_{l,b,a,r,a}$: the three incoming virtual legs from the left, right, and above become the indices l , r , and a , the physical leg is relabeled b , and a trivial auxiliary leg α is appended. By construction, the bond dimensions of l , r , and b legs are either 1 or d , while those of a and α are upper bounded by χ , consistent with the assumption introduced above. Next, we apply the tripartite decomposition of Eq. (B1) to T , obtaining three tensors $A^{[h=1]}$, $B^{[h=1]}$, and $C^{[h=1]}$ (Fig. 7c). Among the resulting legs, only above (a) leg and the newly introduced leg (γ) have the bond dimension χ ; all others retain bond di-

mensions 1 or d . The tensor $B^{[h=1]}$ is then contracted with the tensor directly above $\Psi^{[h=2]}$ along the a leg. This produces a new five-leg tensor one layer higher, whose legs all point inward and respect the assumed bond dimensions (Fig. 7d). Iterating this sequence raises the orthogonality center layer by layer until it reaches the topmost tensor (Figs. 7e and 7f). At this point, the orthogonality surface column has been split into two columns, $\{A^{[h]}\}$ on the left and $\{C^{[h]}\}$ on the right. Finally, each $C^{[h]}$ is contracted with the adjacent tensor $\Phi^{[h]}$; truncating the resulting vertical bond to dimension χ completes the shift of the orthogonality surface by one column (Fig. 7g). We note that the cost of the Moses move is on the order of $O(\chi^3)$. As discussed in Sec. IV A, we use the outcomes of the Moses move as an initial guess for the subsequent alternating linearized variational optimization, in which the solution is refined to reduce errors in the shift [34].

[1] P. W. Anderson, More is different, *Science* **177**, 393 (1972).

[2] P. A. Lee, N. Nagaosa, and X.-G. Wen, Doping a mott insulator: Physics of high-temperature superconductivity, *Rev. Mod. Phys.* **78**, 17 (2006).

[3] M. Z. Hasan and C. L. Kane, Colloquium: Topological insulators, *Rev. Mod. Phys.* **82**, 3045 (2010).

[4] J. I. Cirac, D. Pérez-García, N. Schuch, and F. Verstraete, Matrix product states and projected entangled pair states: Concepts, symmetries, theorems, *Rev. Mod. Phys.* **93**, 045003 (2021).

[5] S. R. White, Density matrix formulation for quantum renormalization groups, *Phys. Rev. Lett.* **69**, 2863 (1992).

[6] S. R. White, Density-matrix algorithms for quantum renormalization groups, *Phys. Rev. B* **48**, 10345 (1993).

[7] U. Schollwöck, The density-matrix renormalization group, *Rev. Mod. Phys.* **77**, 259 (2005).

[8] F. Verstraete and J. I. Cirac, Matrix product states represent ground states faithfully, *Phys. Rev. B* **73**, 094423 (2006).

[9] M. B. Hastings, An area law for one-dimensional quantum systems, *J. Stat. Mech* **2007**, P08024 (2007).

[10] F. Verstraete, V. Murg, and J. Cirac, Matrix product states, projected entangled pair states, and variational renormalization group methods for quantum spin systems, *Adv. Phys.* **57**, 143 (2008).

[11] U. Schollwöck, The density-matrix renormalization group in the age of matrix product states, *Ann. Phys.* **326**, 96 (2011), january 2011 Special Issue.

[12] R. Orús, A practical introduction to tensor networks: Matrix product states and projected entangled pair states, *Ann. Phys.* **349**, 117 (2014).

[13] There are different ways a complexity measure on quantum states can be defined. We adapt the following definition: The complexity of a quantum state $|\Psi\rangle$ is the minimal circuit depth needed to transform the computational basis state to a state $|\Psi'\rangle$ with $\||\Psi\rangle - |\Psi'\rangle\| < \varepsilon$ using only local two-qubit unitaries.

[14] Y.-Y. Shi, L.-M. Duan, and G. Vidal, Classical simulation of quantum many-body systems with a tree tensor network, *Phys. Rev. A* **74**, 022320 (2006).

[15] G. Vidal, Entanglement renormalization, *Phys. Rev. Lett.* **99**, 220405 (2007).

[16] G. Vidal, Class of quantum many-body states that can be efficiently simulated, *Phys. Rev. Lett.* **101**, 110501 (2008).

[17] V. Murg, F. Verstraete, O. Legeza, and R. M. Noack, Simulating strongly correlated quantum systems with tree tensor networks, *Phys. Rev. B* **82**, 205105 (2010).

[18] D. Poulin, A. Qarry, R. Somma, and F. Verstraete, Quantum simulation of time-dependent hamiltonians and the convenient illusion of hilbert space, *Phys. Rev. Lett.* **106**, 170501 (2011).

[19] S.-H. Lin, R. Dilip, A. G. Green, A. Smith, and F. Pollmann, Real- and imaginary-time evolution with compressed quantum circuits, *PRX Quantum* **2**, 010342 (2021).

[20] F. G. Brandão, W. Chemissany, N. Hunter-Jones, R. Kueng, and J. Preskill, Models of quantum complexity growth, *PRX Quantum* **2**, 030316 (2021).

[21] M. P. Zaletel and F. Pollmann, Isometric tensor network states in two dimensions, *Phys. Rev. Lett.* **124**, 037201 (2020).

[22] R. Haghshenas, M. J. O'Rourke, and G. K.-L. Chan, Conversion of projected entangled pair states into a canonical form, *Phys. Rev. B* **100**, 054404 (2019).

[23] K. Hyatt and E. M. Stoudenmire, Dmrg approach to optimizing two-dimensional tensor networks, arXiv preprint arXiv:1908.08833 (2019).

[24] B. Sapler, M. Kawano, M. P. Zaletel, and F. Pollmann, Diagonal isometric form for tensor product states in two dimensions, arXiv preprint arXiv:2507.08080 (2025).

[25] F. Verstraete and J. I. Cirac, Renormalization algorithms for quantum-many body systems in two and higher dimensions, arXiv preprint cond-mat/0407066 (2004).

[26] F. Verstraete, M. M. Wolf, D. Perez-Garcia, and J. I. Cirac, Criticality, the area law, and the computational power of projected entangled pair states, *Phys. Rev. Lett.* **96**, 220601 (2006).

[27] N. Schuch, M. M. Wolf, F. Verstraete, and J. I. Cirac, Computational complexity of projected entangled pair states, *Phys. Rev. Lett.* **98**, 140506 (2007).

[28] I. Arad and Z. Landau, Quantum computation and the evaluation of tensor networks, *SIAM J. Comput.* **39**, 3089 (2010).

[29] G. Vidal, Efficient classical simulation of slightly entangled quantum computations, *Phys. Rev. Lett.* **91**, 147902 (2003).

[30] G. Vidal, Efficient simulation of one-dimensional quantum many-body systems, *Phys. Rev. Lett.* **93**, 040502 (2004).

[31] J. Surace and L. Tagliacozzo, Fermionic Gaussian states: an introduction to numerical approaches, *SciPost Phys. Lect. Notes* **54** (2022).

[32] D. Gottesman, Theory of fault-tolerant quantum computation,

Phys. Rev. A **57**, 127 (1998).

[33] T. Soejima, K. Siva, N. Bultinck, S. Chatterjee, F. Pollmann, and M. P. Zaletel, Isometric tensor network representation of string-net liquids, *Phys. Rev. B* **101**, 085117 (2020).

[34] S.-H. Lin, M. P. Zaletel, and F. Pollmann, Efficient simulation of dynamics in two-dimensional quantum spin systems with isometric tensor networks, *Phys. Rev. B* **106**, 245102 (2022).

[35] Z. Dai, Y. Wu, T. Wang, and M. P. Zaletel, Fermionic isometric tensor network states in two dimensions, *Phys. Rev. Lett.* **134**, 026502 (2025).

[36] Y. Wu, Z. Dai, S. Anand, S.-H. Lin, Q. Yang, L. Wang, F. Pollmann, and M. P. Zaletel, Alternating and gaussian fermionic isometric tensor network states, *PRX Quantum* **6**, 040324 (2025).

[37] W. Kadow, F. Pollmann, and M. Knap, Isometric tensor network representations of two-dimensional thermal states, *Phys. Rev. B* **107**, 205106 (2023).

[38] Y. Wu, S. Anand, S.-H. Lin, F. Pollmann, and M. P. Zaletel, Two-dimensional isometric tensor networks on an infinite strip, *Phys. Rev. B* **107**, 245118 (2023).

[39] M. S. J. Tepaske and D. J. Luitz, Three-dimensional isometric tensor networks, *Phys. Rev. Res.* **3**, 023236 (2021).

[40] L. Slattery and B. K. Clark, Quantum circuits for two-dimensional isometric tensor networks, arXiv preprint arXiv:2108.02792 (2021).

[41] Z.-Y. Wei, D. Malz, and J. I. Cirac, Sequential generation of projected entangled-pair states, *Phys. Rev. Lett.* **128**, 010607 (2022).

[42] D. Malz and R. Trivedi, Computational complexity of isometric tensor-network states, *PRX Quantum* **6**, 020310 (2025).

[43] T. J. Osborne, J. Eisert, and F. Verstraete, Holographic quantum states, *Phys. Rev. Lett.* **105**, 260401 (2010).

[44] S. Gopalakrishnan, Push-down automata as sequential generators of highly entangled states, *J. Phys. A: Math. Theor.* **58**, 055301 (2025).

[45] C. Schön, E. Solano, F. Verstraete, J. I. Cirac, and M. M. Wolf, Sequential generation of entangled multiqubit states, *Phys. Rev. Lett.* **95**, 110503 (2005).

[46] R. Haghshenas, J. Gray, A. C. Potter, and G. K.-L. Chan, Variational power of quantum circuit tensor networks, *Phys. Rev. X* **12**, 011047 (2022).

[47] S. Anand, J. Hauschild, Y. Zhang, A. C. Potter, and M. P. Zaletel, Holographic quantum simulation of entanglement renormalization circuits, *PRX Quantum* **4**, 030334 (2023).

[48] D. Malz, G. Styliaris, Z.-Y. Wei, and J. I. Cirac, Preparation of matrix product states with log-depth quantum circuits, *Phys. Rev. Lett.* **132**, 040404 (2024).

[49] M. Müller-Lennert, F. Dupuis, O. Szehr, S. Fehr, and M. Tomamichel, On quantum rényi entropies: A new generalization and some properties, *J. Math. Phys.* **54**, 122203 (2013).

[50] E. Lubkin, Entropy of an n-system from its correlation with a k-reservoir, *J. Math. Phys.* **19**, 1028 (1978).

[51] D. N. Page, Average entropy of a subsystem, *Phys. Rev. Lett.* **71**, 1291 (1993).

[52] S. K. Foong and S. Kanno, Proof of page's conjecture on the average entropy of a subsystem, *Phys. Rev. Lett.* **72**, 1148 (1994).

[53] D. M. Greenberger, M. A. Horne, A. Shimony, and A. Zeilinger, Bell's theorem without inequalities, *Am. J. Phys.* **58**, 1131 (1990).

[54] W. Dür, G. Vidal, and J. I. Cirac, Three qubits can be entangled in two inequivalent ways, *Phys. Rev. A* **62**, 062314 (2000).

[55] C. Dasgupta and S.-k. Ma, Low-temperature properties of the random heisenberg antiferromagnetic chain, *Phys. Rev. B* **22**, 1305 (1980).

[56] G. Vitagliano, A. Riera, and J. I. Latorre, Volume-law scaling for the entanglement entropy in spin-1/2 chains, *New J. Phys.* **12**, 113049 (2010).

[57] G. Ramírez, J. Rodríguez-Laguna, and G. Sierra, From conformal to volume law for the entanglement entropy in exponentially deformed critical spin 1/2 chains, *J. Stat. Mech.* **2014**, P10004 (2014).

[58] E. Knill, Fermionic linear optics and matchgates, arXiv preprint quant-ph/0108033 (2001).

[59] L. G. Valiant, Quantum circuits that can be simulated classically in polynomial time, *SIAM J. Comput.* **31**, 1229 (2002).

[60] B. M. Terhal and D. P. DiVincenzo, Classical simulation of noninteracting-fermion quantum circuits, *Phys. Rev. A* **65**, 032325 (2002).

[61] R. Jozsa and A. Miyake, Matchgates and classical simulation of quantum circuits, *Proc. R. Soc. A* **464**, 3089 (2008).

[62] R. Jozsa, B. Kraus, A. Miyake, and J. Watrous, Matchgate and space-bounded quantum computations are equivalent, *Proc. R. Soc. A* **466**, 809 (2010).

[63] M. Hebenstreit, R. Jozsa, B. Kraus, S. Strelchuk, and M. Yoganathan, All pure fermionic non-gaussian states are magic states for matchgate computations, *Phys. Rev. Lett.* **123**, 080503 (2019).

[64] R. Morral-Yepes, M. Langer, A. Gammon-Smith, B. Kraus, and F. Pollmann, Disentangling strategies and entanglement transitions in unitary circuit games with matchgates, arXiv preprint arXiv:2507.05055 (2025).

[65] D. Maslov and M. Roetteler, Shorter Stabilizer Circuits via Bruhat Decomposition and Quantum Circuit Transformations, *IEEE Trans. Inf. Theory* **64**, 4729 (2018).

[66] D. Maslov and W. Yang, CNOT circuits need little help to implement arbitrary Hadamard-free Clifford transformations they generate, *npj Quantum Inf.* **9**, 96 (2023).

[67] A. Javadi-Abhari, M. Treinish, K. Krsulich, C. J. Wood, J. Lishman, J. Gacon, S. Martiel, P. D. Nation, L. S. Bishop, A. W. Cross, B. R. Johnson, and J. M. Gambetta, *Quantum computing with Qiskit* (2024), arXiv:2405.08810 [quant-ph].

[68] T. Prosen, General relation between quantum ergodicity and fidelity of quantum dynamics, *Phys. Rev. E* **65**, 036208 (2002).

[69] T. Prosen, Chaos and Complexity of quantum motion, *J. Phys. A: Math. Theor.* **40**, 7881 (2007), arXiv:0704.2247 [quant-ph].

[70] G. Evenbly and G. Vidal, Algorithms for entanglement renormalization, *Phys. Rev. B* **79**, 144108 (2009).

[71] E. G and V. G, Algorithms for Entanglement Renormalization: Boundaries, Impurities and Interfaces, *J. Stat. Phys.* **157**, 931 (2014).

[72] We apply the Jordan-Wigner transformation by taking the fermionic vacuum to be $|++\cdots+\rangle$; equivalently $n_j = (1 - \sigma_j^x)/2$. This choice is related to the conventional one by a global rotation and leaves the physics unchanged, while rendering Eq. (5) purely quadratic in fermions.

[73] K. Kobayashi, B. Sappier, and F. Pollmann, Holographic representation of one-dimensional many-body quantum states via isometric tensor networks, [10.5281/zenodo.17907383](https://doi.org/10.5281/zenodo.17907383) (2025).

[74] P.-A. Absil, R. Mahony, and R. Sepulchre, *Optimization Algorithms on Matrix Manifolds* (Princeton University Press, 2008).

[75] I. A. Luchnikov, M. E. Krechetov, and S. N. Filippov, Riemannian geometry and automatic differentiation for optimization problems of quantum physics and quantum technologies, *New J. Phys.* **23**, 073006 (2021).

[76] M. Hauru, M. Van Damme, and J. Haegeman, Riemannian optimization of isometric tensor networks, *SciPost Phys.* **10**, 040 (2021).

- [77] X. Zhu, A Riemannian conjugate gradient method for optimization on the Stiefel manifold, *Comput. Optim. Appl.* **67**, 73 (2017).
- [78] P.-A. Absil, C. Baker, and K. Gallivan, Trust-Region Methods on Riemannian Manifolds, *Found. Comput. Math.* **7**, 303 (2007).
- [79] J. Townsend, N. Koep, and S. Weichwald, **Pymanopt: A Python Toolbox for Optimization on Manifolds using Automatic Differentiation** (2016), arXiv:1603.03236 [cs].
- [80] J. Bradbury, R. Frostig, P. Hawkins, M. J. Johnson, C. Leary, D. Maclaurin, G. Nocula, A. Paszke, J. VanderPlas, S. Wanderman-Milne, and Q. Zhang, **JAX: composable transformations of Python+NumPy programs** (2018).